Stormtime energy transfer in global MHD simulation

M. Palmroth, T. I. Pulkkinen, and P. Janhunen
Finnish Meteorological Institute, Helsinki, Finland

C.-C. Wu
NASA Goddard Space Flight Center, Greenbelt, Maryland, USA

Received 16 April 2002; revised 5 September 2002; accepted 1 October 2002; published 30 January 2003.

[1] We use a three-dimensional global magnetohydrodynamic (MHD) simulation code to examine the energy flow from the solar wind to the magnetosphere. We simulate a major magnetic storm, which occurred on 6–7 April 2000. During this disturbed period the energy input to the magnetosphere was highly enhanced. For the energy transfer calculation a method for identifying the magnetopause surface from the simulation is developed. We calculate the total energy flux component normal to the magnetopause surface, thus giving the energy flux transferred from the solar wind to the magnetosphere. With this method we identify the locations on the magnetopause surface where significant energy transfer takes place during the storm evolution. During the main phase the energy is transferred from the plane parallel and antiparallel to the interplanetary magnetic field (IMF) clock angle Sunward of $X_{GSE} > -10\ R_E$. During the recovery phase most of the energy is transferred in the low-latitude equatorial sectors Sunward of the dawn-dusk terminator. We discuss the possible explanations to the observed energy transfer locations. We also compare the time evolution of the total transferred energy to the time evolution of the empirical ϵ parameter calculated from the solar wind parameters. During the main phase the total transferred energy in the simulation is well correlated with ϵ, although it is about four times larger. During the recovery phase the total transferred energy and ϵ are not well correlated, and their ratio is much larger than during the main phase. Finally, we discuss limitations of the developed method, which is based on calculating fluxes through surfaces using surface integrals. *INDEX TERMS:* 2784 Magnetospheric Physics: Solar wind/magnetosphere interactions; 2788 Magnetospheric Physics: Storms and substorms; 2753 Magnetospheric Physics: Numerical modeling; 2724 Magnetospheric Physics: Magnetopause, cusp, and boundary layers; 2740 Magnetospheric Physics: Magnetospheric configuration and dynamics; *KEYWORDS:* energy transfer, magnetic storms, magnetopause, solar wind-magnetosphere coupling

Citation: Palmroth, M., T. I. Pulkkinen, P. Janhunen, and C.-C. Wu, Stormtime energy transfer in global MHD simulation, *J. Geophys. Res.*, *108*(A1), 1048, doi:10.1029/2002JA009446, 2003.

1. Introduction

[2] Magnetospheric dynamics is largely controlled by the external driver, the solar wind, and the interplanetary magnetic field (IMF). Internal magnetospheric processes contribute to the details of when and where, e.g., substorms begin and what the exact dynamic sequence will be, but the energy required to power the system is drawn from the interaction with the solar wind, especially during periods of southward IMF [e.g., *Baker et al.*, 1997]. Quantitative assessment of the energy input and dissipation in the magnetosphere, both during magnetospheric substorms and magnetic storms, has been one of the key observational challenges of the International Solar-Terrestrial Physics (ISTP) program [e.g., *Weiss et al.*, 1992; *Lu et al.*, 1998; *Turner et al.*, 2001; *Pulkkinen et al.*, 2003].

0148-0227/03/2002JA009446$09.00

[3] *Akasofu* [1981] was one of the pioneers in evaluating the magnetospheric energy budget during magnetic storms. They parametrized the input in the form of the ϵ parameter, which gives the energy input (in SI units) in watts in the form

$$\epsilon = \frac{4\pi}{\mu_0} V B^2 l_0^2 \sin^4\left(\frac{\theta}{2}\right), \quad (1)$$

where V is the solar wind velocity, B is the IMF intensity, and θ is the IMF clock angle ($\tan(\theta) = B_Y/B_Z$), and $l_0 = 7\ R_E$ is an empirical scaling parameter. They further assumed that the energy is dissipated mainly in the ring current and that only a minor portion would be dissipated in the auroral ionosphere. While the significance of the ionospheric energy dissipation ($\sim$50%) both during magnetospheric storms and substorms has been demonstrated in many studies [*Lu et al.*, 1998; *Tanskanen et al.*, 2002], the ϵ parameter in its original formulation is still the most widely

used energy coupling function in quantitative, empirical energy budget analyses.

[4] The functional form of the ϵ parameter resembles the representation of the solar wind Poynting flux, and hence often the ϵ parameter is interpreted as a transfer function of magnetic energy from the solar wind into the magnetosphere. However, it is to be noted that the functional form is derived empirically and thus does not carry an exact physical interpretation [*Koskinen and Tanskanen*, 2002]. Furthermore, as the scaling parameter l_0 was originally determined by fixing the energy input to equal the estimated energy dissipation, its value becomes uncertain when the values of the energy dissipation in the ring current, ionosphere, and plasmoids have been revised.

[5] Observational evaluation of the global energy budget in the magnetosphere-ionosphere system is a difficult task, as there are as yet no global measurements that would continuously provide direct estimates of the energy dissipation. The ionospheric dissipation can be estimated using the auroral electrojet indices [e.g., *Ahn et al.*, 1983], and the ring current energy density can be estimated from the *Dst* index [*Turner et al.*, 2001], but these give only crude estimates of the very complex system. More accurate determinations require extensive data-based modeling such as the AMIE method for the ionospheric Joule heating and precipitation energy [*Lu et al.*, 1998], or in situ measurements of, e.g., the ring current particle population [*Turner et al.*, 2001]. Detailed understanding of the energy input-dissipation cycle as well as the relative roles of the various dissipation channels and their dependence on the energy input are critical elements in our understanding of the large-scale dynamic behavior of the magnetosphere.

[6] Global MHD simulations provide a means to examine the global energy flow in the coupled solar wind-magnetosphere-ionosphere system, within the limitations of the MHD approach to describe the dynamic processes in the magnetosphere [e.g., *Papadopoulos et al.*, 1999]. The present-day global MHD simulations describe the self-consistent dynamic evolution of the entire system based on upstream solar wind and IMF measurements only. While the solar wind and the magnetosphere are described with ideal MHD equations, the ionosphere is in most cases given as an electrostatic solution solving the potential distribution in the ionosphere, which couples to the magnetosphere via field-aligned currents [e.g., *Fedder and Lyon*, 1995; *Janhunen*, 1996; *Winglee*, 1998]. In the outer magnetosphere, the dynamics is often reproduced quite reliably, as verified by comparisons with in situ spacecraft measurements, while the inner magnetosphere still poses problems, because the overlapping ring current and plasmasphere plasmas cannot be correctly represented by the single-fluid MHD description [e.g., *Pulkkinen et al.*, 1998]. Here we concentrate on one aspect of the energy transport in the MHD simulation, namely the energy flux through the magnetopause surface, and compare that to the observational ϵ parameter during a magnetic storm event.

[7] The magnetic storm on 6–7 April 2000 was driven by a full halo coronal mass ejection (CME) on 4 April 2000 [*Huttunen et al.*, 2002]. The magnetosphere mostly interacted with the sheath region of the interplanetary CME, while signatures of the CME material were not observed until the storm recovery phase. Figure 1 shows a summary

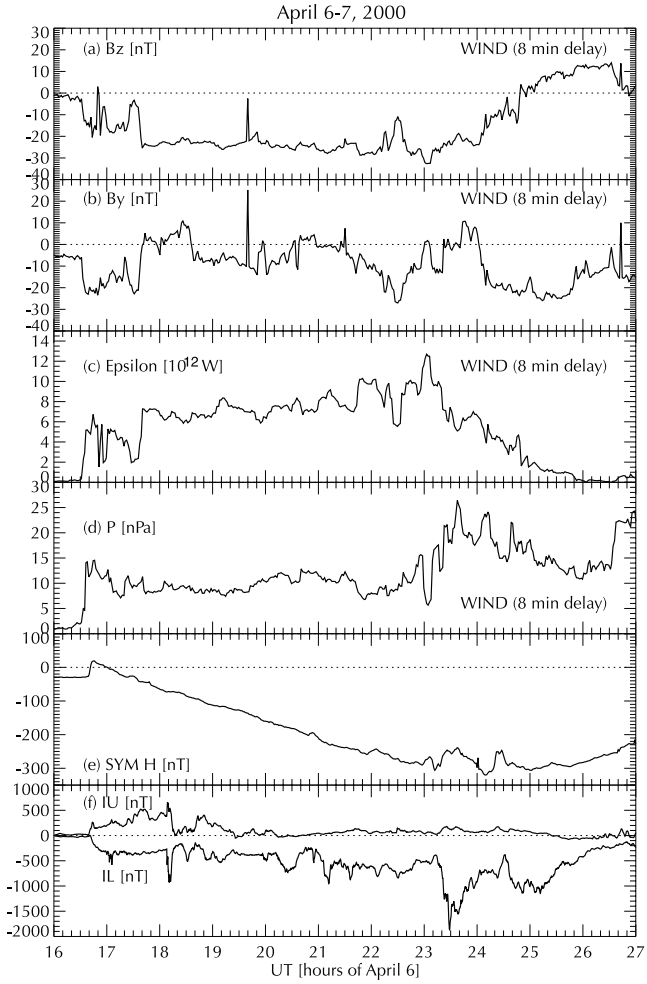

Figure 1. Summary of the solar wind and IMF parameters with the common magnetospheric activity indices during the April 2000 major storm.

of the solar wind and IMF parameters and the following magnetospheric activity. Figures 1a–1b show the strongly southward interplanetary field during 1600–0100 UT and the mostly negative but fluctuating B_Y. The IMF B_X (not shown) is mainly positive, fairly stationary, and mainly below 10 nT. The energy input into the magnetosphere as parametrized by the ϵ parameter was strongly enhanced at the beginning of the storm and was above the storm level input of (10^{12} W) [*Akasofu*, 1981] throughout the southward IMF period (Figure 1c). The solar wind pressure was also unusually high throughout this period (Figure 1d). The storm intensity reached close to −300 nT as measured by the SYM H index (high time resolution *Dst*), and the high-latitude magnetic activities that maximized toward the end of the main phase reached levels of about 2000 nT in the auroral electrojet indices IU/IL derived from the IMAGE magnetometer chain [*Tanskanen et al.*, 2002] (Figure 1e–1f). Thus this was a large storm both in terms of the solar wind driver (large, long-lasting negative IMF B_Z) and in terms of the *Dst* depression well below intense storm level of −100 nT (for more details see *Huttunen et al.* [2002]).

[8] In this paper we examine the energy flow through the magnetopause boundary during the storm event described

above, using the GUMICS-4 global MHD simulation [*Janhunen*, 1996]. We first describe the simulation setup and show the simulation results by comparison to in situ observations in the magnetosphere and in the magnetosheath. We then describe the method for magnetopause identification and the computation of the energy flux. We identify the locations on the magnetopause surface where the energy input takes place during the storm evolution. The energy flux through the magnetopause is shown to be correlated with the ϵ parameter; the differences and similarities are discussed. Finally, we discuss some problems associated with the surface integration within the MHD simulation and end with our conclusions.

2. MHD Simulation of the April 2000 Storm

[9] GUMICS-4 is a global magnetospheric MHD simulation code, which solves MHD equations in fully conservative form in the magnetosphere and solar wind and electrostatic equations in the ionospheric domain [*Janhunen*, 1996]. The conservative form MHD equations guarantee that energy, mass, and momentum are conserved in the simulation. The magnetic field has been decomposed into $\mathbf{B} = \mathbf{B}_0 + \mathbf{B}_1$ [*Tanaka*, 1994], where $\mathbf{B}_0$ is the intrinsic dipole field. The simulation box covers the solar wind out to 32 R_E and the magnetotail out to 224 R_E. The ionosphere is solved in a three-dimensional grid with 20 nonuniform height levels. The ionospheric electron density, affected by the UV radiation from the Sun and the electron precipitation from the magnetosphere, is used in the calculation of the local height-integrated Pedersen and Hall conductivities, which in turn are used in the ionospheric potential calculation together with the field-aligned currents from the magnetosphere. The ionospheric potential mapped to the edge of the magnetospheric domain (3.7 R_E spherical shell) is used as a boundary condition for the MHD equations. GUMICS-4 uses an automatically adaptive Cartesian octogrid in the magnetospheric domain. In the ionospheric domain the triangular grid size is fixed, although refined in the auroral oval region. In this simulation of the April 2000 storm the smallest and largest grid sizes were 0.5 and 8 R_E in the magnetospheric domain, respectively. The densest grid is distributed in regions where the gradients are large, i.e., the bow shock, the magnetopause, and the tail plasma sheet. However, the grid adaptation also depends on location, such that far away from the Earth larger gradients are needed to refine the grid. As a difference to other similar codes, GUMICS-4 uses temporal subcycling, which means that the time step is not constant throughout the simulation box but is smaller in the near Earth region and larger in the distant tail [*Janhunen et al.*, 1996]; this saves both computation time and memory. Elliptic cleaning is used to keep $\nabla \cdot \mathbf{B}$ small [*Brackbill and Barnes*, 1980]. The present simulation results were carried out in a code setup similar to the one used by *Palmroth et al.* [2001].

[10] In this paper we introduce results from an MHD simulation of the storm period on 6–7 April 2000 [*Huttunen et al.*, 2002]. Seventeen hours of solar wind input data were simulated starting from 1400 UT on 6 April 2000. Data from the Wind satellite were used as the upstream boundary condition for the simulation. The interplanetary field B_x was set to zero at the Sunward boundary to ensure

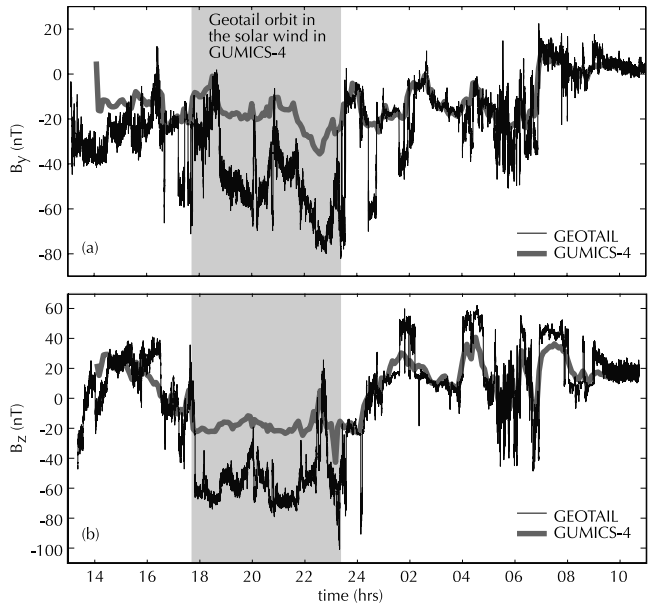

Figure 2. Geotail 3-s calibrated magnetic field data (black) and simulated magnetic field on Geotail orbit (grey): (a) B_y and (b) B_z components.

divergence-free input magnetic field. Wind was located upwind of the magnetosphere, at the time of the storm sudden commencement (SSC) at (55, 39, −6) R_E in the geocentric solar ecliptic (GSE) coordinate system. *Huttunen et al.* [2002] estimated the delay time from Wind to the Earth to be about 8 minutes. The Wind data were not delayed in the simulation, because the solar wind data enters to the simulation box at X = 32 R_E and the solar wind speed was unusually high during this event (∼600 km/s). Thus we estimate that the timing error due to the omission of the time lag is only ∼4 min, which is less than the time interval with which the magnetospheric and ionospheric files are saved (5 min). The SSC was observed at 1640 UT, while in the simulation the SSC occurs between 1635 and 1640 UT.

[11] In the following, we present comparisons of the simulated and measured time series data to validate the model performance. Before the SSC, the Geotail spacecraft crossed the dayside subsolar magnetopause and moved duskward in the equatorial plane magnetosheath. Figure 2 shows the Geotail 3-s calibrated magnetic field measurements [*Kokubun et al.*, 1994] and the GUMICS-4 simulated magnetic field along the Geotail orbit. The measured and simulated B_y and B_z components in Figures 2a and 2b are well correlated, with the exception of the time interval 1800–2300 UT. A closer examination of the Geotail orbit in the simulation box shows that during 1800–2300 UT Geotail location in the simulation was in the solar wind, whereas the measurements show that Geotail did not leave the magnetosheath. The Geotail distance to the bow shock in the simulation after 1800 UT was changing in time but mostly within one grid spacing or less. The discrepancy during 1800–2300 UT may be explained by the fact that in the simulation setup, the dipole tilt angle was set to a constant value, selected to be the tilt angle at 0000 UT on 7 April 2000. This may have caused tilting of the magneto-

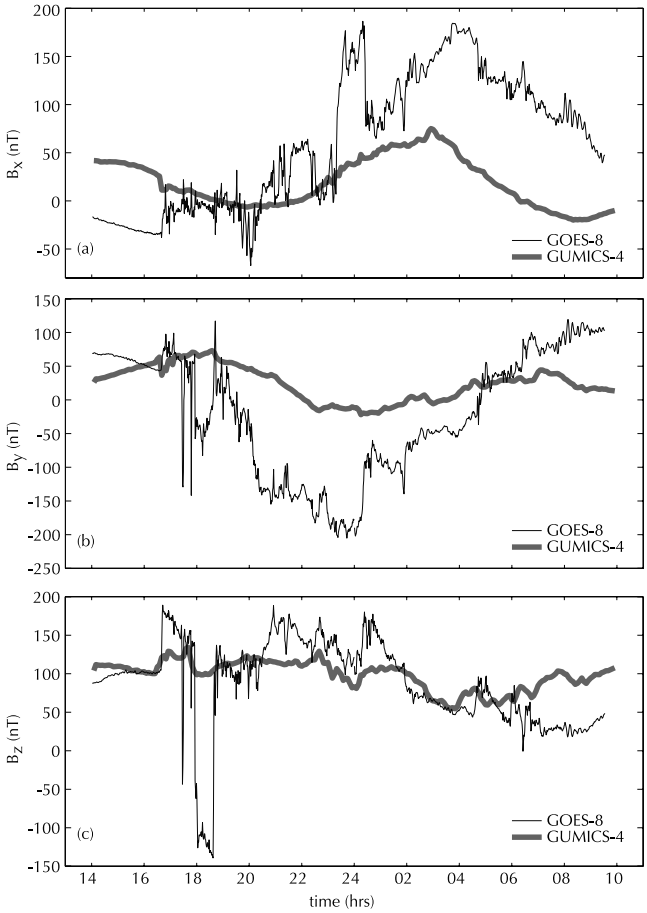

Figure 3. Goes-8 magnetic field data (black) and simulated magnetic field on Goes-8 orbit (grey). (a) B_x, (b) B_y, and (c) B_z components.

sphere such that Geotail orbit reached the solar wind in the simulation.

[12] Figure 3 shows a further data comparison with the simulation results. GOES-8 geostationary spacecraft, located above the United States west coast at 285° longitude, was traversing the dawnside magnetosphere toward the subsolar region at the beginning of the simulated period. The data show that the GOES-8 spacecraft was inside the magnetosphere most of the time, but shortly before 1800 UT the spacecraft emerged into the magnetosheath and stayed there for about an hour. This is best seen in the B_z component (Figure 3c), which was decreased to −100 nT, implying that the spacecraft went out from the dipole-dominated magnetosphere ($B_z > 0$) into a highly compressed solar wind magnetic field and hence the magnetosheath domain. In the simulation, the large scale variations follow the measurements, although with a much smaller amplitude. This has also been noted in other MHD simulations of geostationary orbit magnetic fields [e.g., *Pulkkinen and Wiltberger*, 2000]. Problems with data simulation comparisons in the inner magnetosphere are to be expected because of the vastly different temperatures of the inner magnetosphere plasmas (e.g., the ring current, plasma sheet, and the plasmasphere). The ring current, on the other hand, is highly enhanced during magnetic storms and contributes significantly to the geostationary orbit magnetic field. However, all simulated magnetic field components show a reaction to the SSC at 1640 UT. Furthermore, the simulated B_z component (Figure 3c) follows the observations also in the small scales. For example, the spacecraft dip into the magnetosheath can be recognized, although the intensity of the simulated B_z component shows that the GOES-8 orbit in the simulation only skims the magnetosheath boundary. In fact a close examination of the simulated data shows that the GOES-8 orbit in the simulation was within one grid spacing from the magnetosheath during the time when measurements show a spacecraft dip into the magnetosheath. The discrepancy might again be explained by the constant dipole tilt angle. Given the strongly disturbed period, the agreement especially for the B_z component is quite good for an MHD simulation.

[13] Figure 4 shows the subsolar magnetopause distance computed using the empirical model by *Shue et al.* [1998] (black line) and in the GUMICS-4 simulation as determined from the boundary of open and closed magnetic field lines (grey line) and the magnetopause currents (j_y, dashed line). The *Shue et al.* [1998] model gives the subsolar magnetopause distance based on the IMF B_z component and the solar wind dynamic pressure. In Figure 4, the solar wind parameters have been evaluated from the simulation outside the bow shock to facilitate comparison of the *Shue et al.* [1998] model and the simulation results. The magnetopause determination from the j_y currents was done visually using current density surfaces at the noon-midnight meridian plane. The open-closed field line boundary was searched automatically from the simulation. Both methods of the subsolar magnetopause identification have been introduced by *Palmroth et al.* [2001]. All three curves in Figure 4 show a rapid decrease at the time of the SSC, after which the subsolar distances remain small until 0000 UT and the start of the storm recovery phase. After 0000 UT during the northward IMF period, the GUMICS open-closed field line boundary and the *Shue*

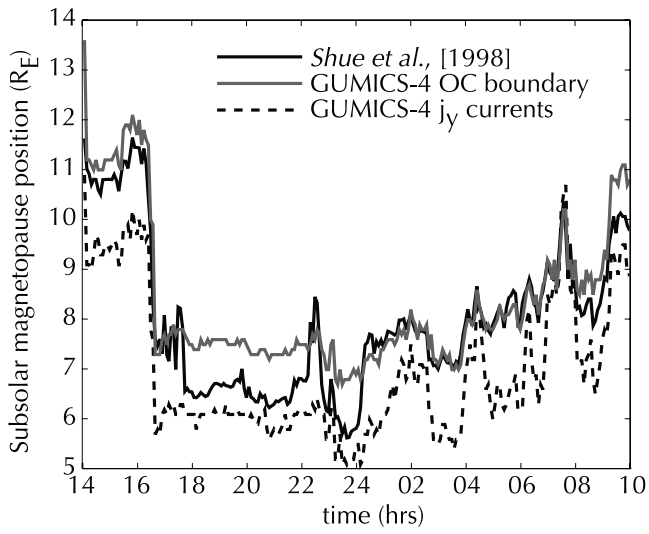

Figure 4. Subsolar magnetopause distance in the *Shue et al.* [1998] model and in the GUMICS-4 simulation determined from the open-closed magnetic field line boundary and the magnetopause currents.

et al. [1998] subsolar distance show almost a one-to-one correspondence with each other.

[14] As the *Shue et al.* [1998] is instantaneous and empirical model, the stand-off distance does not have a ''magnetospheric memory'' but reacts immediately to changes in the solar wind. In magnetospheric MHD simulations the large spatial size and the various current systems introduce inertial effects for the reorganization of the magnetopause current distributions and thus for the subsolar magnetopause distance. Thus it is expected that the GUMICS-4 subsolar distances remain at approximately the same location during the storm main phase, whereas the *Shue et al.* [1998] subsolar distance shows considerable variation. During the southward IMF period, the GUMICS-4 subsolar distance is further Sunward when determined from the open-closed field line boundary, whereas the j_y current maximum is closer to the Earth as compared with the *Shue et al.* [1998] model; this has also been noted before [*Palmroth et al.*, 2001]. However, the time variations of the two differently determined subsolar distances are quite similar and overall agree well with the *Shue et al.* [1998] model [*Palmroth et al.*, 2001; *Janhunen and Palmroth*, 2001].

3. Magnetopause Surface Identification From MHD Simulation

[15] Evaluation of the solar wind energy transfer to the magnetosphere requires a definition of an appropriate surface, the magnetopause. In this section, the magnetopause is searched from the simulation by finding the solar wind streamlines encompassing the magnetosphere. A set of streamlines is created at $X_{GSE} = +15\ R_E$, well outside the bow shock. The streamline grid is defined in the $Y_{GSE}Z_{GSE}$ plane in a 50 by 50 R_E box with the X_{GSE} axis at the center. The distance between neighboring streamlines is 0.5 R_E along each axis, giving in total 10,000 streamlines.

[16] At the beginning of the magnetopause search, the set of 10,000 streamlines is mapped 0.5 R_E in the anti-Sunward direction. For each 0.5 R_E step in the $-X_{GSE}$ direction, the algorithm searches for a void of streamlines starting from the X_{GSE} axis. Finding such a void of streamlines indicates that the streamlines have started to bend around the magnetosphere. When the void becomes larger than 1 R_E, the algorithm finds an inner boundary, which defines the magnetopause in the $Y_{GSE}Z_{GSE}$ plane. The search for the inner boundary starts by dividing the $Y_{GSE}Z_{GSE}$ plane into 10° sectors. In each sector the streamlines are sorted by their radius $\sqrt{Y_{GSE}^2 + Z_{GSE}^2}$ from the X_{GSE} axis. Three closest streamlines are excluded, and the magnetopause is defined to be the arithmetic mean of the radii of the four next closest streamlines. The three closest streamlines are excluded from the magnetopause determination because some streamlines may enter the magnetosphere and would hence produce erroneous results, which was clearly seen when the method was tested. However, varying the number of streamlines excluded from the evaluation and the number of streamlines used to compute the mean produced only small changes to the magnetopause location, which gives confidence to the selected method. With this procedure, the resulting resolution of the magnetopause surface is 0.5 R_E in the X_{GSE} direction and 10° in the $Y_{GSE}Z_{GSE}$ plane. Figure 5 illustrates the quality of the used magnetopause search method compared with the plasma density from the GUMICS-4 simulation; the streamline-searched magnetopause coincides sufficiently well with the density gradients, which would be another way to define the magnetopause. However, our tests show that the density gradients especially in the magnetotail are not sufficiently sharp for an automated surface recognition.

[17] The magnetopause search is carried out in the $Y_{GSE}Z_{GSE}$ plane until X_{GSE} reaches $-30\ R_E$. Note that although the subsolar position is a point on the X_{GSE} axis, the magnetosphere itself needs not to be aligned with the X_{GSE} axis, and the magnetospheric boundary in the $Y_{GSE}Z_{GSE}$ plane is not necessarily circular. In fact, in the 6–7 April 2000 storm simulation the magnetosphere is elliptic in the $Y_{GSE}Z_{GSE}$ plane and not aligned with the X_{GSE} axis. Figure 6 shows examples of the calculated magnetopause surfaces. The time shown was selected around the SSC (1640 UT), the time interval between the panels is 5 min. Figure 6 illustrates clearly how radically and globally the magnetopause is deformed when the interstellar cloud hits the magnetosphere [*Huttunen et al.*, 2002].

4. Energy Flow Through Magnetopause in MHD Simulation

[18] When the surface coordinates are known, the energy flow across each quadrangular surface element defined by the surface grid can be computed. First, we calculate the area of the surface element and a surface vector perpendicular to the element. In practice, the quadrangular surface element is divided into two triangles, and the areas and surface vectors are computed separately for the two triangles. The area of the surface element is then the sum of the areas of the two triangles, and the surface vector perpendicular to the element is the vector average of the surface vectors for the two triangles. The energy flux dE_q across the quadrangular surface element is then

$$dE_q = dA\mathbf{K} \cdot \hat{\mathbf{n}}, \tag{2}$$

where dA is the area of the surface element and $\hat{\mathbf{n}}$ is the unit vector perpendicular to the surface element; the vector points outwards from the magnetopause. $\mathbf{K}$ is the total energy flux, and is defined as

$$\mathbf{K} = \left(U + P - \frac{B^2}{2\mu_0}\right)\mathbf{v} + \frac{1}{\mu_0}\mathbf{E} \times \mathbf{B}, \tag{3}$$

where U is the total energy density, P is the pressure, $\mathbf{B}$ is the magnetic field, $\mathbf{v}$ is velocity, $\mathbf{E}$ is the electric field, and $\mathbf{E} = \mathbf{B} \times \mathbf{v}$. The total energy flux $\mathbf{K}$ is interpolated from the GUMICS-4 MHD simulation at the center of each surface element. The total energy flux through the surface is then the sum of the energy fluxes of each surface element,

$$E_s = \int dE_q \tag{4}$$

[19] In Figure 6 the color-coding represents the energy flow across the surface elements around the time of the

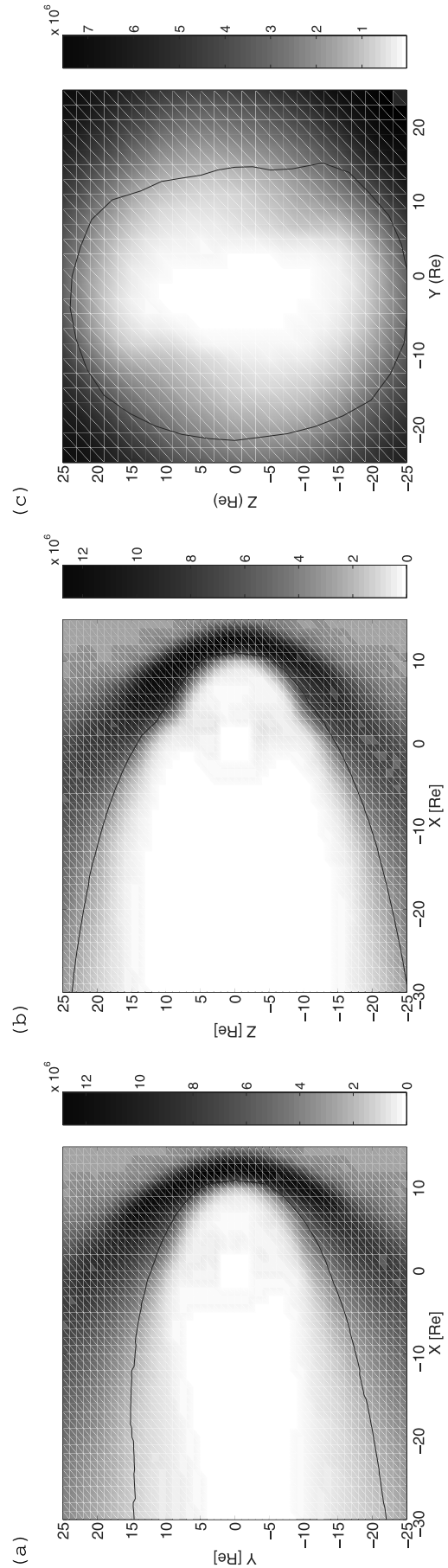

Figure 5. The density color-coded from the GUMICS simulation and the magnetopause surface using the streamline search method in (a) $X_{GSE}Y_{GSE}$ plane, (b) $X_{GSE}Z_{GSE}$ plane, and (c) $Y_{GSE}Z_{GSE}$ plane, $X_{GSE} = -30\ R_E$. See color version of this figure at back of this issue.

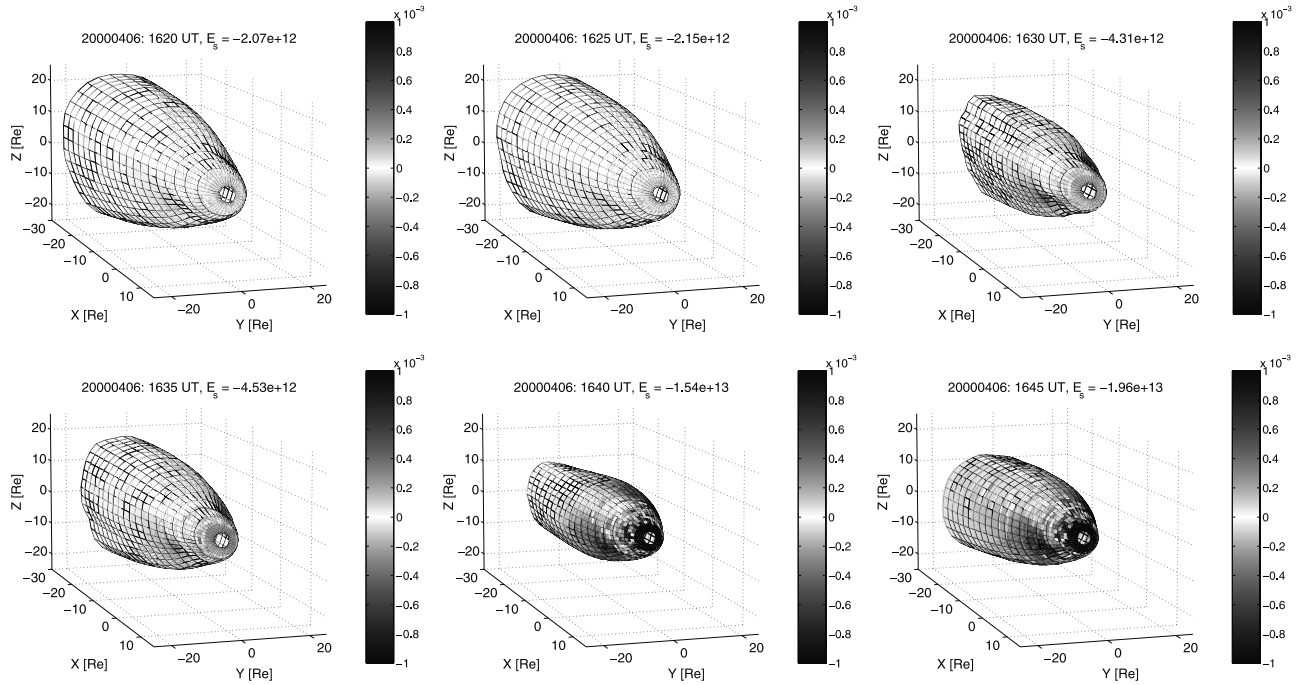

Figure 6. The GUMICS-4 magnetopause surfaces around the time of the SSC (1640 UT) defined from mapping the solar wind streamlines. Color-coded is the energy flux through the surface. See color version of this figure at back of this issue.

SSC; all panels are plotted using the same color scale. The small hole in the subsolar region is caused by the plotting routine. The energy flowing into the magnetosphere is represented by blue colors and negative values, whereas positive values and red colors represent the energy flow out from the magnetosphere; white colors indicate the areas where the energy flux is close to zero.

[20] In Figure 6, at 1620 UT, 20 min before the SSC, the surface is quite smooth; only the cusps show as depressions on the surface. Globally, the energy flux is small, although locally a modest amount of energy comes in through the cusps. At 1630 UT the surface is already deformed; this is because the shock foot has arrived at the magnetopause. The energy flux is slightly enhanced, the cusps show now more energy inflow, and directly in front of them is a region of slight energy outflow. At 1635 UT, the shock foot deformation has diminished, but still the energy flux remains at the same level as in the previous time step. At 1640 UT the SSC effect is clearly visible, the size of the entire magnetosphere has decreased, the surface is deformed, and the energy flux has strongly increased. The cusps show a large inflow area, and again directly in front of particularly the southern cusp there is a strong energy outflow area. The subsolar region, however, contains strong energy inflow. At 1645 UT the surface has recovered to its bullet-like shape after the strong deformation, but the energy flux remains at an enhanced level similarly to the previous time step.

[21] Figure 7 presents the total energy flow through the surface (E_s) calculated using equation (4) during the storm evolution. Also plotted is the experimental ϵ parameter calculated from the observed solar wind parameters. Note that we have plotted the absolute value of E_s to facilitate the comparison with the ϵ parameter. During the main phase of the storm, E_s calculated from the simulation and the ϵ parameter show similar behavior, only E_s is about four times larger than ϵ. At the SSC time, ϵ increases approximately to half of its maximum during the storm evolution, whereas E_s increases first to a level characteristic of the main phase, decreases then to smaller values, and rises again to values similar to those obtained at the SSC arrival. While the behavior of both curves during the main phase is similar, the recovery phase shows some differences: The ϵ parameter decreases to very small values as the IMF B_z turns positive. At the IMF B_z turning, E_s decreases only slightly and does not reach values preceding the storm. There are two enhance-

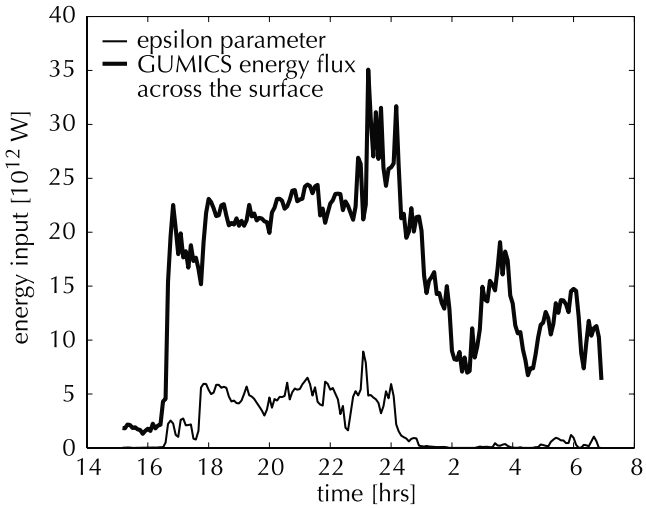

Figure 7. Total energy flux through the magnetopause surface in the simulation and the experimental ϵ parameter calculated from the solar wind parameters.

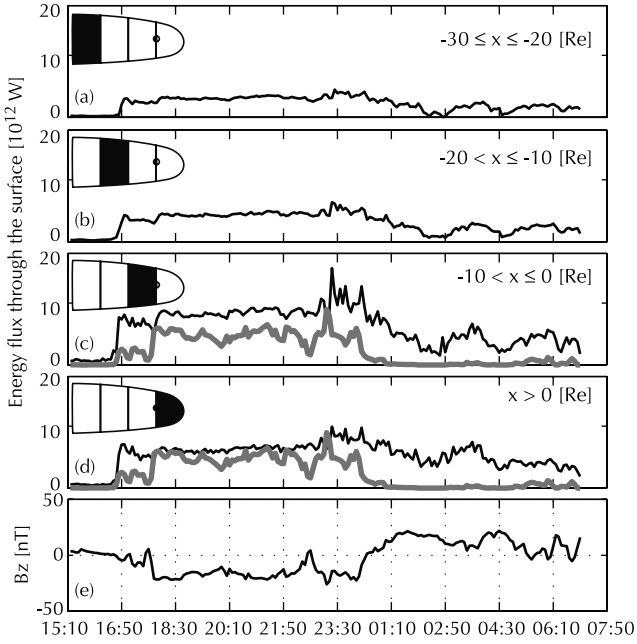

Figure 8. Total energy flux through the magnetopause surface in the X_{GSE} axis in the simulation integrated over the $Y_{GSE}Z_{GSE}$ plane. (a) E_s in $-30\ R_E \leq X_{GSE} \leq -20\ R_E$, (b) E_s in $-20\ R_E < X_{GSE} \leq -10\ R_E$, (c) E_s in $-10\ R_E < X_{GSE} \leq 0\ R_E$, ϵ plotted with grey, (d) E_s in $X_{GSE} > 0\ R_E$, ϵ plotted with grey, (e) IMF B_z component.

ments of energy transfer during the recovery phase, which are also seen as minor enhancements in the ϵ parameter.

[22] Figure 8 illustrates the location of the magnetopause surface where the energy transfer takes place in the X_{GSE} direction; the energy fluxes through surface elements are integrated over the $Y_{GSE}Z_{GSE}$ plane and separated by their X_{GSE} value. Figure 8a shows E_s in the outermost slice in the tail at $-30\ R_E \leq X_{GSE} \leq -20\ R_E$, Figure 8b gives E_s at $-20\ R_E < X_{GSE} \leq -10\ R_E$, Figure 8c gives E_s at $-10\ R_E < X_{GSE} \leq 0\ R_E$, Figure 8d gives E_s at $X_{GSE} > 0\ R_E$, and Figure 8e shows the IMF B_z. In Figures 8c and 8d the ϵ parameter, calculated from the solar wind parameters, is also plotted (grey). Figure 8 shows that during the main phase, most of the energy enters the magnetosphere in the region $X_{GSE} \geq -10\ R_E$, tailward of this distance the energy transfer rate is decreased. Note that the subsolar distance is very close to the Earth during the main phase (see Figure 4), giving a much smaller area to the surface in Figure 8d relative to the other slices during the storm main phase. Therefore the total energy flux is smaller in Figure 8d than in Figure 8c, even though the energy flux per unit area would be larger at the dayside magnetopause during the main phase. During the recovery phase, however, the energy flux decreases in all the surface slices excluding the $X_{GSE} > 0\ R_E$ (Figure 8d), where the energy flux stays almost at the same level as during the main phase. The surface slice $-10\ R_E < X_{GSE} \leq 0\ R_E$ (Figure 8c) shows only two periods of slightly enhanced energy flux during the recovery phase (around 0345 and 0530 UT), and as can be seen from Figure 8e, at those times the IMF B_z is close to zero or even slightly negative.

[23] Figure 9 presents the azimuthal distribution of the energy transfer, now all the X_{GSE} values are integrated and the panels are separated by their azimuth angle (ϕ). Figures 9a–9f show the energy transfer in the sectors $0° \leq \phi < 60°$, $60° \leq \phi < 120°$, $120° \leq \phi < 180°$, $180° \leq \phi < 240°$, $240° \leq \phi < 300°$, and $300° \leq \phi < 360°$, respectively. Figure 9g shows the IMF clock angle $\tan(\theta) = B_y/B_z$. During the main phase, the largest energy transfer rates are seen in Figures 9a and 9d, whereas the lowest energy transfer rates are seen in Figures 9c and 9f. The low-latitude equatorial sectors (Figures 9b and 9e) show almost steady energy transfer during the storm evolution; no apparent change from the storm main phase to the recovery phase can be seen in the energy transfer rates in these sectors. At the time of the SSC and directly after it, the equatorial sectors show largest energy transfer, and as can be seen from Figure 9g, the IMF clock angle is also in this sector. Furthermore, Figure 9g shows that during the storm main phase the clock angle was predominantly in the sector $180° \leq \phi < 240°$; correspondingly, the largest energy transfer was in this sector. Also the sector 180° away from the clock angle shows enhanced energy transfer rates. Sectors 90° away from the clock angle show the lowest energy transfer rates during the storm main phase. During the storm recovery phase, however,

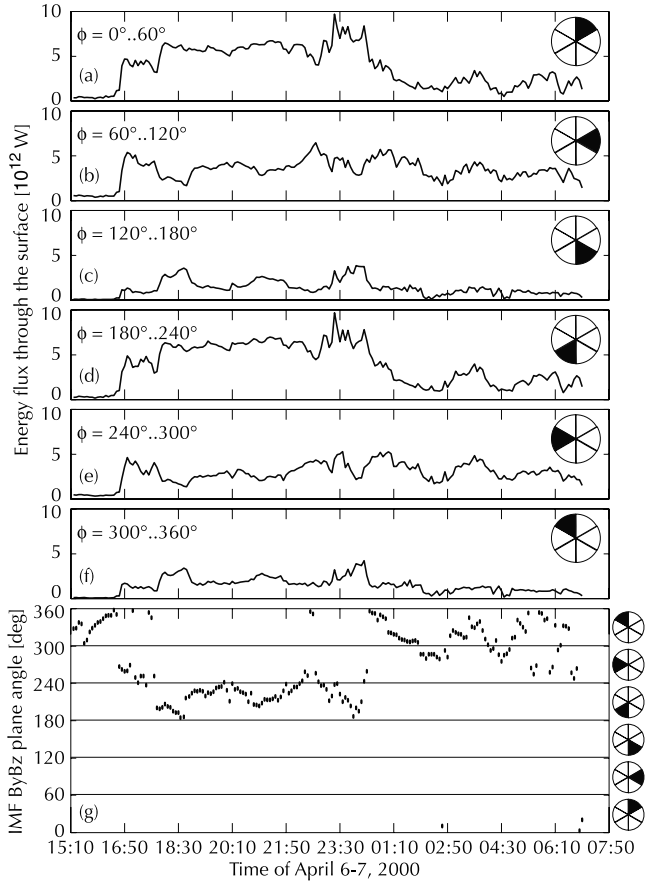

Figure 9. Total energy flux integrated over the X_{GSE} axis. (a) E_s in $0° \leq \phi < 60°$, (b) E_s in $60° \leq \phi < 120°$, (c) E_s in $120° \leq \phi < 180°$, (d) E_s in $180° \leq \phi < 240°$, (e) E_s in $240° \leq \phi < 300°$, (f) E_s in $300° \leq \phi < 360°$. (g) The angle between the IMF B_yB_z plane and the Z_{GSE} axis.

when the clock angle was predominantly in the $240° \leq \phi < 360°$ sector, it is not evident that the energy transfer would take place in that sector. On the contrary, it seems that low-latitude equatorial sectors and sectors that also contributed the most during the main phase show more enhanced energy transfer rates.

5. Verification of Numerical Method

[24] To validate the method described above for calculating fluxes through surfaces in the simulation, we created spheres with random radii and random locations (inside, outside, and intersecting the magnetosphere), and calculated the mass flux, energy flux, and magnetic flux through them. Figures 10a, 10b, and 10c present the results for the relative mass, energy, and magnetic fluxes, respectively, plotted against the radius of the sphere. By relative flux we mean the quantity

$$\frac{\oint d\mathbf{A} \cdot \mathbf{F}}{\oint dA|\mathbf{F}|}, \tag{5}$$

where $\mathbf{F}$ is one of ($\rho\mathbf{v}$, $\mathbf{K}$, $\mathbf{B}$). Thus equation (5) gives the percentage of how conservative the quantity is on average. Figures 10a and 10b show that the mass and energy fluxes over a closed surface are up to 10% positive on average, suggesting that spurious mass and energy are generated inside the spheres. Figure 10c, however, shows that the magnetic flux over a closed surface is close to zero on average, illustrating that $\nabla \cdot \mathbf{B} = 0$ is well maintained.

[25] The apparent nonconservation of energy and mass flux through a closed surface in a conservative MHD simulation may be disturbing at first glance. The conservation of magnetic flux is most probably a consequence of the periodic removal of the magnetic field divergence, which is carried out by the MHD code. The fact that the magnetic flux is conservative through the closed surface but the mass and energy fluxes are not, when the same computing method is used in calculating the surface integrals, suggests that there are no programming errors in the surface integral and interpolation codes. This leads us to believe that the source of the discrepancies is in the MHD numerical method itself.

[26] In the MHD simulations using Godunov-type method [e.g., *Janhunen*, 1996; *Powell et al.*, 1999], when calculating the continuity equation of a variable (e.g., $\partial\rho/\partial t = -\nabla(\rho\mathbf{v})$), an estimate of the mass flux is established at the faces of the cells, after which the mass within the cubical cell is updated. This method is conservative in the sense that mass is not lost. However, there is no guarantee that the conservative $\rho\mathbf{v}$ at the cell faces is the average of $\rho\mathbf{v}$ of the neighboring cells. In the Roe-type method [e.g., *LeVeque*, 1992; *Janhunen*, 2000] used in this code, the flux at the cell faces is obtained by linearizing the MHD equations locally in the vicinity of the face, solving the linear problem exactly, and calculating the flux at the cell face corresponding to the obtained linear solution. The result is only approximately the average of $\rho\mathbf{v}$ of the neighboring cells. Therefore the result depends nonlinearly on the right and left cell states, which might explain the apparent non-conservation of $\rho\mathbf{v}$ and $\mathbf{K}$. As mentioned before, the reason for the good conservation of the magnetic flux is probably the regular removal of the magnetic divergence, which is done by estimating the cell face magnetic flux by the average of the magnetic flux of the neighboring cells. Thus for the magnetic flux there is no nonlinearity.

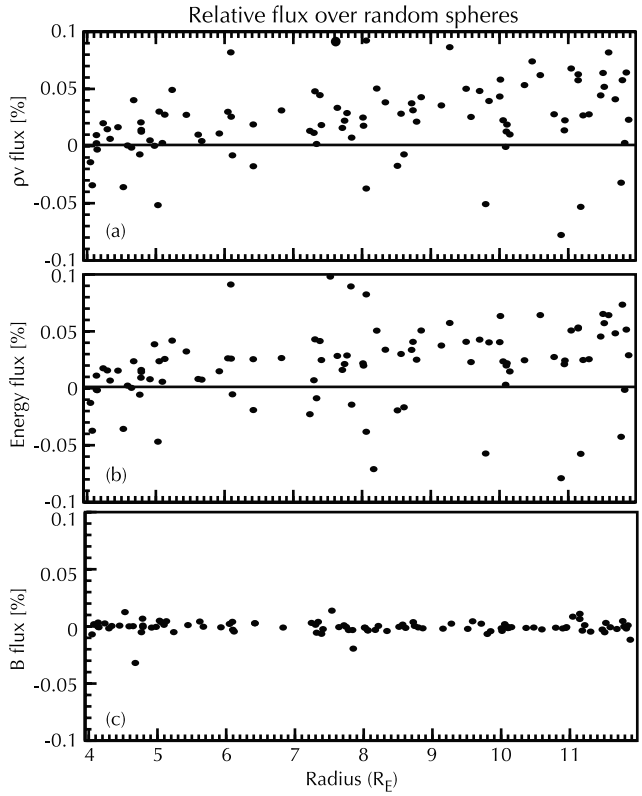

Figure 10. Relative fluxes over random spheres plotted against the sphere radius. (a) Mass flux, (b) energy flux, and (c) magnetic flux.

[27] A desirable MHD numerical method would exactly conserve mass, momentum, and energy, preserve $\nabla \cdot \mathbf{B} = 0$, and guarantee positivity of pressure and density. Our finite volume method almost satisfies these requirements because it is conservative and positivity-maintaining and uses elliptic cleaning to achieve $\nabla \cdot \mathbf{B} = 0$. As explained above, a property of Godunov-type methods is that there is no exact numerical counterpart of Gauss' theorem, because the interface fluxes with respect to which the method is conservative depend nonlinearly on the touching cell states. Only by using the numerical cell face fluxes in the surface integral would Gauss' theorem become valid, but then the surface should follow cell boundaries, which is not what we want here. Using a classical finite volume method where the interface fluxes are linear functions of the left and right states, e.g., the Lax-Friedrichs or Lax-Wendroff method, would restore Gauss' theorem but yield an unacceptably large numerical diffusion. For these reasons, the method introduced in this paper is not directly applicable to closed surfaces. In other words, the total energy content transferred through a surface cannot be calculated reliably using surface integrals (but could be computed using volume integrals). Nonetheless, the method is still fully usable on open surfaces. Therefore, the question addressed in this paper, ''Where on the magnetopause surface does the energy

transfer take place'' is fully answerable using the method described here.

6. Discussion

[28] In this paper we have described a method with which the total energy transfer from the solar wind into the magnetosphere can be investigated using a global MHD simulation. This is not the first study to consider energy transfer from the solar wind into the magnetosphere in a global MHD simulation. There are a few studies where Poynting flux has been mapped from the solar wind into the magnetosphere [*Walker et al.*, 1993; *Ashour-Abdalla et al.*, 1999; *Papadopoulos et al.*, 1999]. However, this is the first time the energy flux has been mapped quantitatively, since we have used a conservative quantity, the total energy flux, instead of a non-conservative quantity, the Poynting flux. Mapping Poynting flux flow lines gives an indication of the paths of Poynting flux through the surface and in the magnetosphere, but it does not specify the amount of energy transferred along these paths. We have also compared the total transferred energy with other experimental quantities. Furthermore, in the Poynting flux mapping studies, the main finding has been the focusing of the Poynting flux inside the magnetosphere. In this study, we can actually identify the locations on the magnetopause surface, where the energy transfer takes place and study their dependence on the solar wind parameters.

[29] Owing to the numerical method used in GUMICS-4 MHD simulation, we cannot investigate the energy flux through a closed surface with the developed method; however, energy flux through an open surface can be investigated. The quantity representing the sum of energy flux through an open surface, E_s, overestimates the energy that is left into the magnetosphere. This is because the magnetospheric volume bounded by the surface bears extra energy that only shortly visits the magnetosphere before flowing back to the solar wind, or maybe even energy of the magnetosheath (because of uncertainties of the surface location). This is especially true for the energy flux near the flanks, where the total energy vector is more or less parallel to the magnetopause surface.

[30] The most critical phase of the calculation of the transferred energy from the solar wind into the magnetosphere is the definition of the magnetopause. We tested four methods: pressure and density gradient maxima, current density maximum, and the streamline method. We found that the pressure and density gradient and current density methods typically give less smooth surfaces than the streamline method. A likely reason is that the streamlines are obtained by integrals of MHD variables, whereas the two other methods use derivatives. However, apart from different smoothness properties, the surfaces produced by the different methods are consistent with each other. The magnetopause defined from the streamlines is consistent with e.g., the density gradient, as can be seen from Figure 5. Regarding observations, the GOES-8 data comparison (Figure 3) revealed that the observed spacecraft dip to the magnetosheath was modeled sufficiently well with GUMICS-4. Also the *Shue et al.* [1998] model is consistent with the GUMICS-4 magnetopause (Figure 4). Given these facts and restrictions, we believe that the defined magnetopause is reasonably well located, and therefore also the calculated energy flux through the magnetopause should be sufficiently accurate.

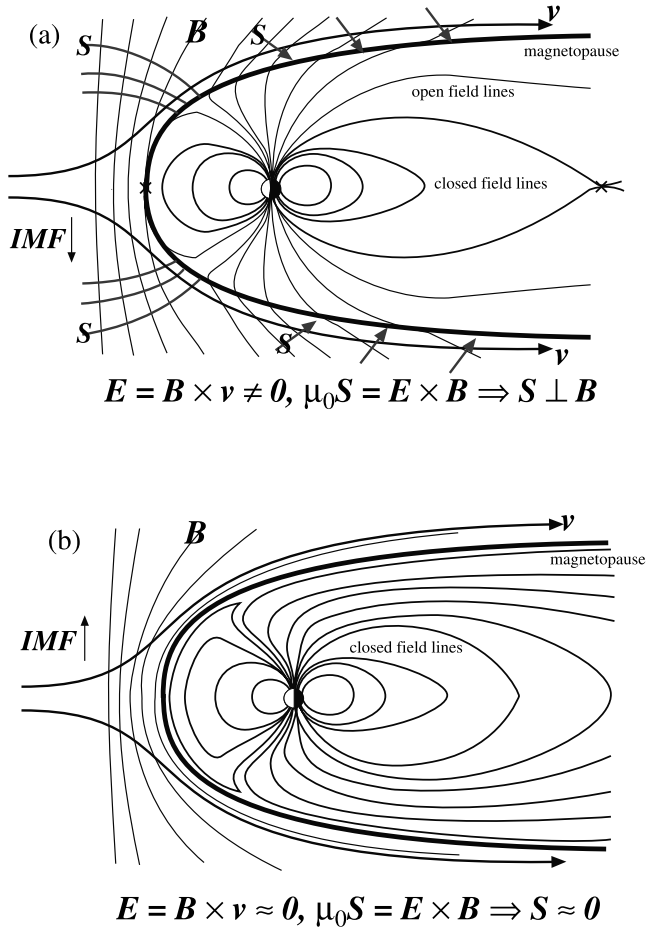

Figure 11. (a) Schematic of the energy transfer during southward IMF. Bold black lines are the closed field lines, thin black lines are the open field lines, and grey lines are the Poynting flux. See text for explanation. (b) As in Figure 11a but for northward IMF. See text for explanation.

[31] Our simulation results show that during the main phase the energy transfer occurs in the plane parallel and antiparallel to the IMF clock angle sunward of $X_{GSE} = -10$ R_E. The sectors perpendicular to the plane of the IMF clock angle show the weakest energy transfer during the storm main phase. Figure 11a presents a schematic drawing of the energy transfer during southward IMF based on the results in this paper. During southward IMF practically the whole dayside is open owing to reconnection [e.g., *Luhmann et al.*, 1984; *Kallio and Koskinen*, 2000]. Once the dipole field line has merged with the solar wind field line at the dayside reconnection region, it stays open until it reaches the tail reconnection region. Therefore energy may enter freely on the open field lines sunward of the tail reconnection region, consistent with our results in Figures 8c and 8d.

[32] As illustrated in Figure 11a, the dipole field lines merged with the solar wind field lines traverse tailward with a finite angle with the magnetosheath velocity field. As $\mathbf{E} = \mathbf{B} \times \mathbf{v}$, and $\mu_0\mathbf{S} = \mathbf{E} \times \mathbf{B}$ ($\mathbf{S} \perp \mathbf{B}$), the Poynting vector $\mathbf{S}$ has a component towards the magnetosphere at the magneto-

pause. Furthermore, the Poynting flux focuses towards the magnetosphere in the plane parallel to the IMF clock angle and deviates around the magnetosphere in the plane perpendicular to the IMF clock angle [*Papadopoulos et al.*, 1999; *Koskinen and Tanskanen*, 2002]. This explains the azimuthal energy transfer locations during the main phase; the sectors parallel and antiparallel to the IMF clock angle gain most of the Poynting flux focused towards the magnetosphere. On the basis of our study it is evident that the Poynting flux focusing in the plane of the IMF controls the energy transfer locations during the storm main phase; otherwise equal amount of energy would be transferred at each sector.

[33] During the recovery phase of the storm most of the energy in the simulation is transferred sunward of the dawn-dusk terminator and from the sectors to which the IMF clock angle is not directed. Most of the energy comes from the low-latitude equatorial sectors. There are two time periods around 0345 and 0530 UT, when also the surface slice $-10\ R_E < X_{GSE} \leq 0\ R_E$ contributes to the energy transfer, during these times the energy flux is also enhanced in sectors $0° \leq \phi < 60°$ and $180° \leq \phi < 240°$. During these time periods the IMF B_z is close to zero or negative (Figure 8e) explaining the enhanced energy flux.

[34] Figure 11b shows that during northward IMF there are no magnetic field lines that have a large component normal to the magnetopause. The magnetosheath magnetic and velocity fields encompass the magnetosphere, and are almost parallel to each other everywhere else other than in the subsolar region. Therefore the electric field component at the magnetopause is close to zero, and hence the Poynting flux must also be close to zero everywhere at the magnetopause other than in the subsolar region. At the subsolar region, however, the magnetopause might not be open in the direction where the Poynting flux focuses, and therefore the Poynting flux focusing in the plane of the IMF clock angle does not appear to be the controlling factor in the energy transfer during the recovery phase, which is consistent with our result that during the recovery phase the energy is not transferred in the plane parallel and antiparallel to the IMF clock angle.

[35] In contrast, it appears that the location of the reconnection regions is the controlling factor of the energy transfer during the recovery phase. *Kallio and Koskinen* [2000] give the location of the largest shear between the magnetosheath and magnetospheric field lines in the equatorial sectors, when the IMF clock angle is in the sector 240° to 300°, accounting for the observed energy transfer in the low-latitude equatorial sectors. The smallest amount of energy transfer in the sectors parallel and antiparallel to the IMF clock angle can be explained when looking at Figure 6h of *Kallio and Koskinen* [2000]; there is almost no shear between the magnetosheath and magnetospheric field lines, and thus reconnection and energy transfer is likely to be weak in these sectors regardless of the focusing Poynting flux.

[36] The energy transfer from the solar wind to the magnetosphere is traditionally estimated by the ϵ parameter [*Akasofu*, 1981]. Owing to its functional form, ϵ has sometimes been referred to as the upstream Poynting flux transfer function, although in this case only the perpendicular component of the magnetic field should be used in equation (1). In the derivation of ϵ the solar wind input has been scaled to the magnetospheric and ionospheric output, which means that ϵ represents the energy content transferred from the solar wind and dissipated in the magnetosphere. Hence it is not strictly appropriate to compare ϵ to E_s in this study, since E_s is the energy transferred into the magnetosphere but not entirely left there. This is because we have not considered the energy flux through the back wall of the magnetopause surface in the tail. Nonetheless, the time evolution of E_s and ϵ are very similar, at least during the storm main phase. During the storm recovery phase ϵ is close to zero, but E_s remains enhanced. A clear distinction between E_s and ϵ can be seen during the storm SSC. While E_s increases to values also characteristic of the main phase, ϵ increases only to approximately half of its maximum during the main phase. This difference is probably due to enhanced solar wind dynamic pressure; a parameter that is present in the functional form of ϵ only through the solar wind speed.

[37] Since E_s and ϵ are so similar during the main phase, it seems evident that the Poynting flux is the controlling factor of the energy transfer into the magnetosphere, as originally put forth by *Akasofu* [1981]. However, the solar wind itself carries very little energy with the Poynting flux compared to the energy carried by the bulk flow. In the magnetosheath, however, the energy carried by the bulk flow is almost tangential to the magnetopause, and therefore is not likely to transfer into the magnetosphere. Furthermore, in the magnetosheath, the magnetic field compresses and the solar wind speed decelerates, and therefore $\mathbf{v}$ and $\mathbf{B}$ are not the same as the solar wind parameters used in the calculation of ϵ. Anyway, it appears that the energy contributing to the magnetospheric processes resembles the functional form of the Poynting flux, and it has actually been generated at the bow shock, because the Poynting flux carried by the solar wind would hardly be enough to supply all the magnetospheric processes [*Koskinen and Tanskanen*, 2002]. Because of these contradictions, the role of ϵ in the energy transfer from the solar wind into the magnetosphere needs to be further examined. The method described in this paper is only the first step in trying to quantify physically the energy transfer function; in the future the method must be further developed to take into account also the dissipated energy, which is the right parameter to be compared with ϵ.

7. Summary

[38] The main results of this paper are the following: (1) A robust method for identifying the magnetopause surface has been developed. As an application, the total energy flux component from the solar wind into the magnetosphere has been calculated through the surface during a major magnetic storm. (2) Evaluation of the energy flux through the surface shows that during the main phase (southward IMF) the Poynting flux focusing in the plane of the IMF clock angle controls the location of the energy transfer. (3) During the recovery phase (northward IMF) the Poynting flux focusing in the plane of the IMF clock angle does not play a major role in determining the energy transfer locations. (4) During the main phase the time evolution of the energy transfer rate is well correlated with the time evolution of the ϵ parameter. During the main phase the ratio E_s/ϵ is about 4, while during the recovery phase it is much larger.

[39] **Acknowledgments.** We thank the NSSDC for maintaining the CDAWeb facility through which the input data for the simulation were obtained. We thank Hannu Koskinen and Esa Kallio for useful discussions on the theory of the energy transfer. The work of M.P. and P.J. is supported by the MaDaMe program of the Academy of Finland.

[40] Lou-Chuang Lee and Chin S. Lin thank Raymond J. Walker for his assistance in evaluating this paper.

References

Ahn, B.-H., S.-I. Akasofu, and Y. Kamide, The Joule heat production rate and the particle energy injection rate as a function of the geomagnetic indices AE and AL, *J. Geophys. Res.*, *88*, 6275–6287, 1983.

Akasofu, S.-I., Energy coupling between the solar wind and the magnetosphere, *Space Sci. Rev.*, *28*, 121–190, 1981.

Ashour-Abdalla, M., M. El-Alaoui, V. Peroomian, and R. J. Walker, Localized reconnection and substorm onset on Dec. 22, 1996, *Geophys. Res. Lett.*, *26*, 3545–3548, 1999.

Baker, D. N., T. I. Pulkkinen, M. Hesse, and R. L. McPherron, A quantitative assessment of energy storage and release in the Earth's magnetotail, *J. Geophys. Res.*, *102*, 7159–7168, 1997.

Brackbill, J. U., and D. C. Barnes, The effect of nonzero $\nabla \cdot B$ on the numerical solutions of the magnetohydrodynamic equations, *J. Comput. Phys.*, *35*, 426, 1980.

Fedder, J. A., and J. G. Lyon, The Earth's magnetosphere is 165 R_E long: Or self-consistent currents, convection, magnetospheric structure and processes for northward interplanetary magnetic field, *J. Geophys. Res.*, *100*, 3623–3635, 1995.

Huttunen, K. E. J., H. E. J. Koskinen, T. I. Pulkkinen, A. Pulkkinen, M. Palmroth, H. Singer, and G. D. Reeves, April 2000 magnetic storm: Solar wind driver and magnetospheric response, *J. Geophys. Res.*, *107*(A12), 1440, doi:10.1029/2001JA009154, 2002.

Janhunen, P., GUMICS-3—A global ionosphere-magnetosphere coupling simulation with high ionospheric resolution, in *Proc. Environmental Modelling for Space-Based Applications, Sept. 18–20 1996*, *Eur. Space Agency Spec. Publ., ESA SP-392*, 233–239, 1996.

Janhunen, P., A positive conservative method for magnetohydrodynamics based on HLL and Roe methods, *J. Comput. Phys.*, *160*, 649–661, 2000.

Janhunen, P., and M. Palmroth, Some observational phenomena are well reproduced by our global MHD while others are not: Remarks on what, why and how, *Adv. Space Res.*, *28*, 1685–1691, 2001.

Janhunen, P., H. E. J. Koskinen, and T. I. Pulkkinen, A new global ionosphere-magnetosphere coupling simulation utilizing locally varying time step, in *Proceedings of Third International Conference on Substorms (ICS 3), Versailles, France, May 12–17*, *Eur. Space Agency Spec. Publ., ESA SP-389*, 205–210, 1996.

Kokubun, S., T. Yamamoto, M. H. Acuna, K. Hayashi, K. Shiokawa, and H. Kawano, The GEOTAIL magnetic field experiment, *J. Geomag. Geoelectr.*, *46*, 7–22, 1994.

Kallio, E. J., and H. E. J. Koskinen, A semiempirical magnetosheath model to analyze the solar wind-magnetosphere interaction, *J. Geophys. Res.*, *105*, 27,469–27,479, 2000.

Koskinen, H. E. J., and E. I. Tanskanen, Magnetospheric energy budget and the epsilon parameter, *J. Geophys. Res.*, *107*(A11), 1415, doi:10.1029/2002JA009283, 2002.

LeVeque, R. J., *Numerical Methods for Conservation Laws*, Birkhäuser Boston, Cambridge, Mass., 1992.

Lu, G., et al., Global energy deposition during the January 1997 magnetic cloud event, *J. Geophys. Res.*, *103*, 11,685–11,694, 1998.

Luhmann, J. G., R. J. Walker, C. T. Russell, N. U. Crooker, J. R. Spreiter, and S. S. Stahara, Patterns of potential magnetic field merging sites on the dayside magnetopause, *J. Geophys. Res.*, *89*, 1739–1742, 1984.

Palmroth, M., P. Janhunen, T. I. Pulkkinen, and W. K. Peterson, Cusp and magnetopause locations in global MHD simulation, *J. Geophys. Res.*, *106*, 29,435, 2001.

Papadopoulos, K., C. Goodrich, M. WIltberger, R. Lopez, and J. G. Lyon, The physics of substorms as revealed by the ISTP, *Phys. Chem. Earth, Part C*, *24*, 189–202, 1999.

Powell, K. G., P. L. Roe, T. J. Linde, T. I. Gombosi, and D. L. Zeeuw, A solution-adaptive upwind scheme for ideal magnetohydrodynamics, *J. Comput. Phys.*, *154*, 284–309, 1999.

Pulkkinen, T. I., and M. Wiltberger, Thin current sheet evolution as seen in observations, empirical models, and MHD simulations, *Geophys. Res. Lett.*, *27*, 1363–1366, 2000.

Pulkkinen, T. I., D. N. Baker, M. Wiltberger, C. Goodrich, J. G. Lyon, and R. E. Lopez, Pseudobreakup and substorm onset: Observations and MHD simulations compared, *J. Geophys. Res.*, *103*, 14,847–14,854, 1998.

Pulkkinen, T. I., N. Y. Ganushkina, E. I. Tanskanen, G. Lu, D. N. Baker, N. E. Turner, T. A. Fritz, J. F. Fennell, and J. Roeder, Energy dissipation during a geomagnetic storm: May 1998, *Adv. Space Res.*, in press, 2003.

Shue, J.-H., et al., Magnetopause location under extreme solar wind conditions, *J. Geophys. Res.*, *103*, 17,691–17,700, 1998.

Tanaka, T., Finite volume TVD scheme on an unstructured grid system for three-dimensional MHD simulation of inhomogenous systems including strong background potential fields, *J. Comput. Phys.*, *111*, 381–389, 1994.

Tanskanen, E. I., T. I. Pulkkinen, H. E. J. Koskinen, and J. A. Slavin, Substorm energy budget near solar minimum and maximum: 1997 and 1999 compared, *J. Geophys. Res.*, *107*(A6), 1086, doi:10.1029/2001JA900153, 2002.

Turner, N. E., D. N. Baker, T. I. Pulkkinen, J. L. Roeder, J. F. Fennell, and V. K. Jordanova, Energy content in the stormtime ring current, *J. Geophys. Res.*, *106*, 19,149–19,156, 2001.

Walker, R. J., T. Ogino, J. Raeder, and M. Ashour-Abdalla, A global magnetohydrodynamic simulation of the magnetosphere when the interplanetary mahnetic field is southward: The onset of magnetotail reconnection, *J. Geophys. Res.*, *98*, 17,235–17,249, 1993.

Weiss, L. A., P. H. Reiff, J. J. Moses, R. A. Heelis, and D. B. Moore, Energy dissipation in substorms, in *Substorms 1*, *ESA SP-335*, pp. 309–317, Eur. Space Agency, Paris, 1992.

Winglee, R. M., Multifluid simulations of the magnetosphere: The identification of the geopause and its variation with IMF, *Geophys. Res. Lett.*, *25*, 4441–4444, 1998.

P. Janhunen, M. Palmroth, and T. I. Pulkkinen, Finnish Meteorological Institute, Geophysical Research, P.O. Box 503, Helsinki, 00101, Finland. (pekka.janhunen@fmi.fi; minna.palmroth@fmi.fi; tuija.pulkkinen@fmi.fi)

C.-C. Wu, NASA Goddard Space Flight Center, Mail Code 696, Greenbelt, MD USA. (ccwu@lepvax.gsfc.nasa.gov)

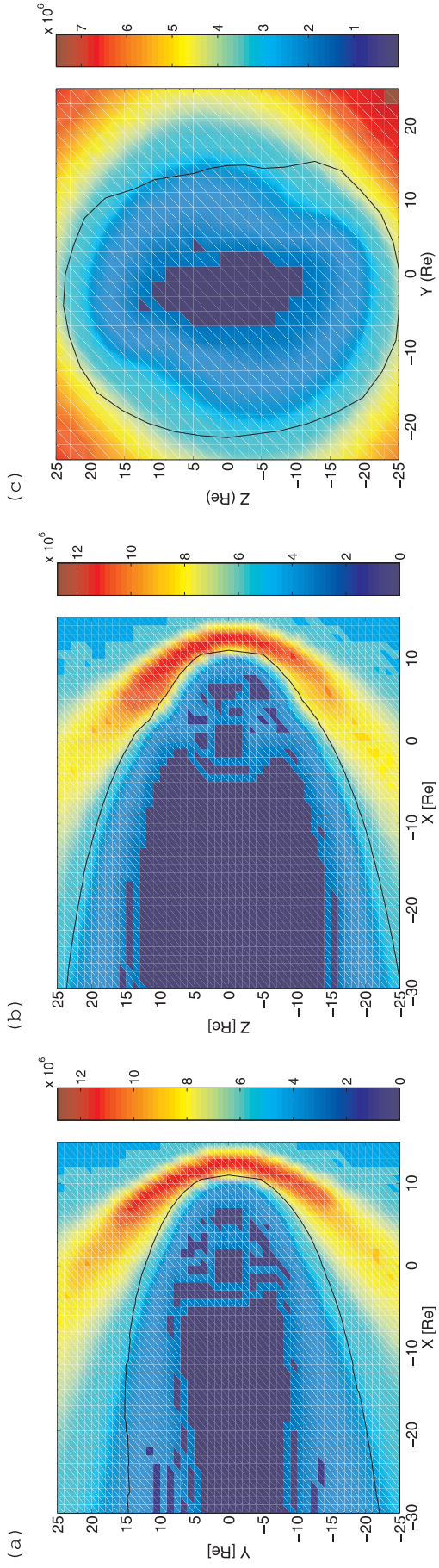

Figure 5. The density color-coded from the GUMICS simulation and the magnetopause surface using the streamline search method in (a) $X_{GSE}Y_{GSE}$ plane, (b) $X_{GSE}Z_{GSE}$ plane, and (c) $Y_{GSE}Z_{GSE}$ plane, $X_{GSE} = -30\ R_E$.

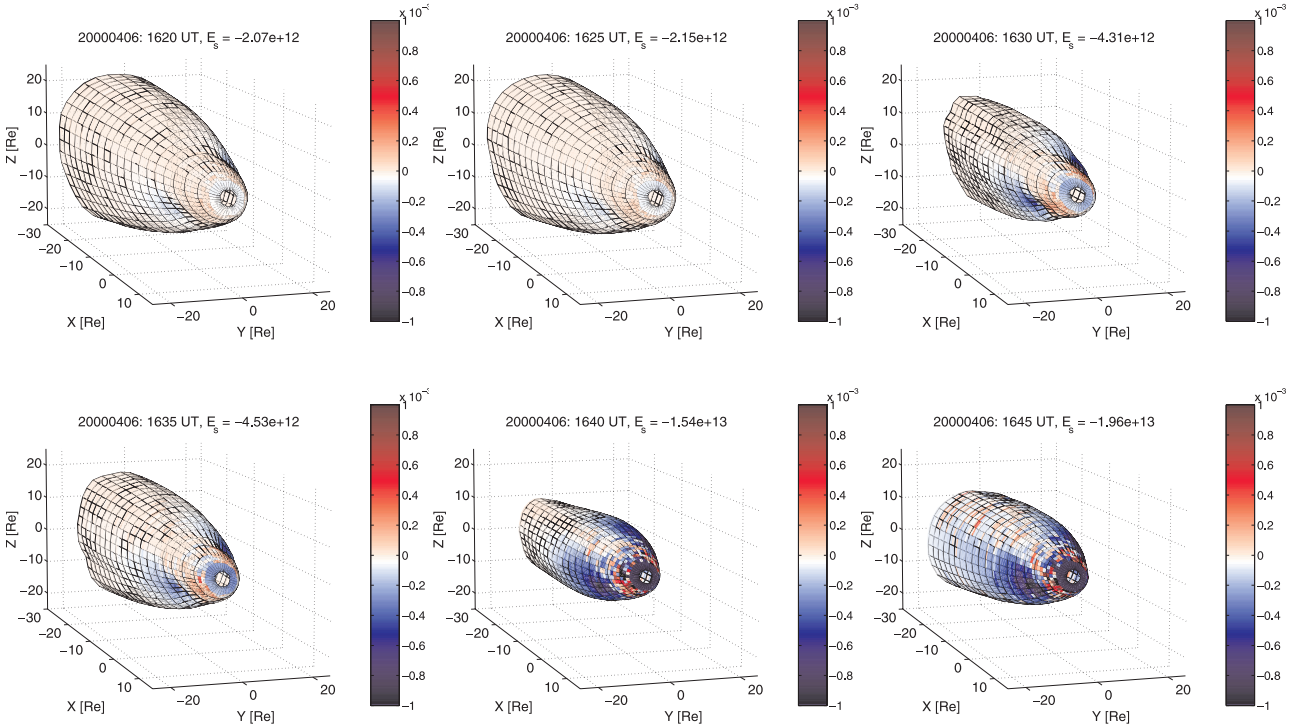

Figure 6. The GUMICS-4 magnetopause surfaces around the time of the SSC (1640 UT) defined from mapping the solar wind streamlines. Color-coded is the energy flux through the surface.